

# Hyperbolicity and Shadowing Directions of a Turbulent 3-D Flow

Angxiu Ni<sup>1</sup>†

<sup>1</sup>Department of Mathematics, University of California, Berkeley, Berkeley, CA 94720, USA

(Received xx; revised xx; accepted xx)

This paper uses compressible flow simulation to analyze the hyperbolicity and shadowing directions of a weakly turbulent 3-D cylinder flow at Reynolds number 525 and Mach number 0.1.

By computing the first 40 Covariant Lyapunov Vectors (CLV), we find that unstable CLVs are active in the near wake region, whereas stable CLVs are active in the far wake region. This phenomenon shows that CLVs point to different directions, which further suggests that general open fluid systems may satisfy some form of hyperbolicity.

By the Non-Intrusive Least Squares Shadowing (NILSS) algorithm, we compute shadowing directions and sensitivities of long-time averaged objectives. Our results suggest that shadowing methods may be valid for general chaotic fluid problems.

**Key words:** Chaotic Flow, Wake, Turbulence, Shadowing, Covariant Lyapunov Vectors, Non-Intrusive Least Squares Shadowing (NILSS), Sensitivity Analysis

---

## 1. Introduction

The chaotic dynamics of many fluid problems, such as turbulence and vortex streets, are central to many important challenges facing science and technology. These chaotic flows are typically controlled by system parameters, such as the incoming flow conditions, or the boundary geometry. This paper studies the 3-D flow past a cylinder at Reynolds number 525 from a dynamical system point of view. More specifically, we study perturbations in flow fields due to perturbations in initial conditions and system parameters, those are, Covariant Lyapunov Vectors (CLV) and shadowing directions of this flow problem.

Chaotic fluid systems depend sensitively on initial conditions: perturbations whose norms grow like exponential functions are called Covariant Lyapunov Vectors (CLV), and their exponents are the Lyapunov Exponents (LE) (Katok & Hasselblatt 1997). Unstable CLVs determines the uncertainty in predicting the future behavior of the dynamical system, provided the past trajectory is known up to a precision (Young 2003). More importantly, unstable CLVs can be regarded as chaotic degrees of freedom (DOF) to whom the apparent complicated behavior can be attributed. This reduction in DOF allows reduced-order numerical methods, such as those developed by Chorin *et al.* (2002); Parish & Duraisamy (2017). In experiments, we can infer some properties of CLVs by reconstructed attractors (Sieber 1987), but more details can be obtained only numerically. In particular, Keefe *et al.* (1992) computed the LE spectrum of turbulent Poiseuille flow. Recently, LE spectrum for some 3-D CFD problems were studied (Blonigan *et al.* 2016a; Fernandez & Wang 2017a).

† Email address for correspondence: niangxiu@math.berkeley.edu

There remains questions about active areas of CLVs in ‘open’ flows, or developing flows such as boundary layers, jets and wakes. Since perturbations in open flows are typically convected downstream, it is difficult to form an intuitive visualization of the CLVs. In contrary, for ‘closed’ flows such as Benard convection and Taylor-Couette flow, global dynamics are expressed at all spatial locations, and CLVs can be effectively interpreted as eigenmodes (Keefe *et al.* 1992). Fernandez & Wang (2017*b*) plotted flow fields of CLVs in an open flow, and they found no significant difference in active areas among CLVs, perhaps because only a few CLVs were computed. However, in this paper, we are able to observe the difference in active areas for different CLVs.

Hyperbolicity is a property of dynamical systems which says the unstable and stable CLVs are bounded away from each other. Uniform hyperbolicity is assumed in many theoretical results, such as the existence of a steady distribution (Young 2002), linear response formula (Ruelle 1997, 2008), and shadowing lemma (Bowen 1970; Pilyugin 1999). However, many chaotic fluid systems are not strictly hyperbolic. For a Kolmogorov flow simulated with 224 DOF (Inubushi *et al.* 2012) and for a 3-D Boussinesq equations simulated with  $5 \times 10^5$  DOF (Xu & Paul 2016), researchers found both cases are not even partially hyperbolic because the angles between CLVs can be very small. Currently, there are not many results regarding hyperbolicity for CFD simulated 3-D Navier-Stokes fluid systems. In this paper, our fluid system is not uniform hyperbolic but is barely partially hyperbolic, and we find a more robust form of hyperbolicity for our fluid system.

Still, it has been conjectured those theoretical results can still be applied on most chaotic systems (Gallavotti & Cohen 1995; Gallavotti 2006; Ruelle 1980). Supports of such conjectures can be found in (Albers & Sprott 2006; Reick 2002; Ni & Wang 2017). In this paper, we are particularly interested in whether shadowing methods are still valid, since shadowing methods typically assumes uniform hyperbolicity, but our fluid problem does not satisfy such assumption.

For a chaotic system, if we coordinate carefully perturbations on both initial conditions and parameters, we can find a shadowing trajectory which remains close to the old trajectory (Bowen 1970). The first order approximation of the difference between the two trajectories is the shadowing direction (Pilyugin 1997). Shadowing methods enable sensitivity analysis of long-time averaged objectives (Wang *et al.* 2014), which is useful in design (Jameson 1988), control (Bewley 2001), inverse problems (Tromp *et al.* 2005), error estimation (Becker & Rannacher 2001; Giles & Süli 2002; Fidkowski & Darmofal 2011), and data assimilation (Thepaut & Courtier 1991). Shadowing is difficult to observe experimentally, and the only method we are aware of is numerical. The theory for shadowing methods typically assumes uniform hyperbolicity, however, in this paper, we show that shadowing directions also exist for our fluid system.

The Least Squares Shadowing method (LSS) (Wang 2014; Wang *et al.* 2014) computes sensitivities of long-time averaged objectives via computing the shadowing direction. With high cost, LSS has been successfully applied in 2-D CFD problems (Blonigan *et al.* 2016*b*). The Non-Intrusive Least Squares Shadowing (NILSS) method (Ni *et al.* 2016; Ni & Wang 2017) reformulates LSS by constraining computation to the unstable subspace. For many real-life problems, NILSS can be hundreds or thousands times faster than LSS. One variant of NILSS is the adjoint, as developed by Blonigan (2017), and by Ni (2018*b,a*). Another variant is the Finite Difference NILSS (FD-NILSS) algorithm (Ni *et al.* 2018), whose implementation requires only primal solvers. In this paper, we use FD-NILSS to compute shadowing directions and sensitivities of our problem.

We begin the main part of the paper by describing the physical and numerical setup for our flow problem. Then the rest of the paper consists of two logically connected parts. First, we review LEs and CLVs, and compute LEs and CLVs for our flow problem.

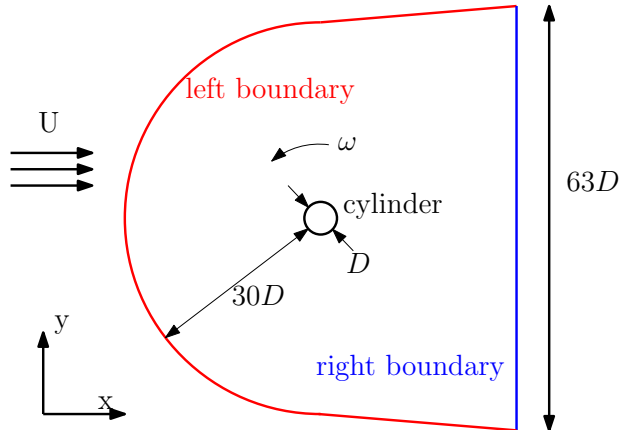


Figure 1: Geometry used in the simulation of a 3-D flow past a cylinder. The spanwise extent of the computational domain is  $Z = 2D$ . The positive direction of the cylinder rotational speed  $\omega$  is counter-clockwise.

The CLV results indicate some form of hyperbolicity, which encourages us to proceed to the second part of the paper, where we review shadowing directions and the FD-NILSS algorithm, using which we compute shadowing directions and sensitivities of several long-time averaged objectives.

## 2. Problem setup and verification of simulation

Our physical problem of the 3-D flow past a cylinder is the same as in (Ni *et al.* 2018). The front view of the geometry of the entire flow field is shown in figure 1. In the rest of the paper, the units we have in mind are SI units, but since in this paper all values are normalized, and in the software all equations are dimensionless, readers may take any compatible set of units. The diameter of the cylinder is  $D = 0.25 \times 10^{-3}$ . The spanwise width is  $Z = 2D$ . The freestream conditions are: density  $\rho_0 = 1.18$ , pressure  $P_0 = 1.01 \times 10^5$ , temperature  $T_0 = 298$ , dynamic viscosity  $\mu = 1.86 \times 10^{-5}$ . The freestream flow is in the x-direction, with the velocity  $U$  being one of the system parameters, and for the base case  $U_0 = 33.0$ . The flow-through time  $t_0$ , defined as the time for  $U_0$  flowing past the cylinder, is  $t_0 = D/U_0 = 7.576 \times 10^{-6}$ . The Reynolds number of the base case is  $Re = \rho_0 U_0 D / \mu = 525$  and Mach number is 0.1. The cylinder can rotate around its center with rotational speed  $\omega$ , which is the second system parameter for our problem.  $\omega$  is measured in round per unit time, and its positive direction is counter-clockwise, as shown in figure 1. For the cylinder to rotate one cycle per flow-through time, the rotation speed  $\omega_0 = 1/t_0 = 1.32 \times 10^5$ .

We run our simulations on two sets block-structured hexahedra meshes. The coarser mesh has  $3.7 \times 10^5$  cells, and finer mesh has  $7.5 \times 10^5$  cells. 2-D slices of the finer mesh are shown in figure 2. For both meshes, the spanwise direction have 48 cells. The CFD solver we use is CharLES developed at Cascade Technologies (Brès *et al.* 2017), using which we perform under-resolved Direct Numerical Simulation (uDNS) without turbulence model. The accuracy of the solver is formally second order in space and third order in time. The spanwise boundaries use periodic boundary conditions; the left boundary uses a convective boundary condition (Coloniuss *et al.* 1993); the right boundary uses the Navier-

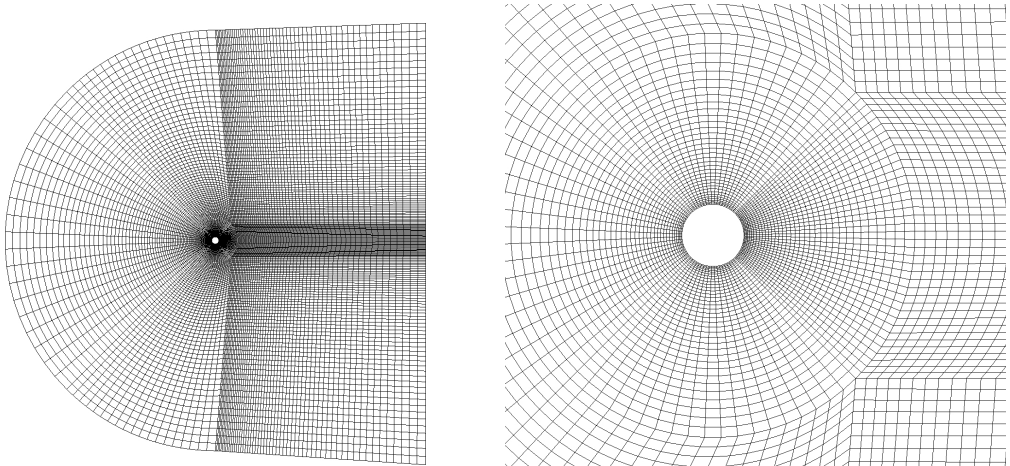


Figure 2: Left: 2-D slice of the finer mesh over the entire computational domain. Right: zoom around the cylinder. This is a block-structured mesh with  $7.5 \times 10^5$  hexahedra. The spanwise direction has 48 cells.

---

	$S_t$	$C_D$
Coarser mesh with $3.7 \times 10^5$ cells	0.21	1.22
Finer mesh with $7.5 \times 10^5$ cells	0.21	1.19
2-D simulation by Mittal & Balachandar (1996)	0.22	1.44
3-D simulation by Mittal & Balachandar (1996)	0.22	1.24
experiment by Williamson & Roshko (1990)	0.21	1.15

Table 1: Comparison with previous literature in the Strouhal number  $S_t$  and the averaged drag coefficient  $C_D$ .

---

Stokes characteristic boundary conditions (NSCBC) boundary condition (Poinsot & Lele 1992). The time step size is  $\Delta t = 10^{-8} = 1.32 \times 10^{-3} t_0$ .

2-D snapshots of the flow field simulated with above numerical settings on the finer mesh are shown in figure 3. The flow is chaotic and 3-D. We also plotted a time averaged flow field in figure 4. As we can see, the computed flow field generally fits our fluid intuitions in the stagnant area before and after the cylinder, the acceleration area around the cylinder, and the boundary layer and wake structures.

We compare our results with previous literature. The same physical problem has been investigated in experiments by Williamson & Roshko (1990), and in numerical simulations by Mittal & Balachandar (1996). We compare the Strouhal number  $S_t$  and the averaged drag coefficient  $C_D$ . Here the Strouhal number is defined by  $S_t = fD/U$ , where  $f$  is the main frequency of the vortex shedding, represented by the history of the lift; the drag coefficient  $C_D = D_r / (0.5\rho_0 U^2 DZ)$ , where  $D_r$  is the drag. As shown in table 1, our results on both meshes match previous experimental and numerical results.

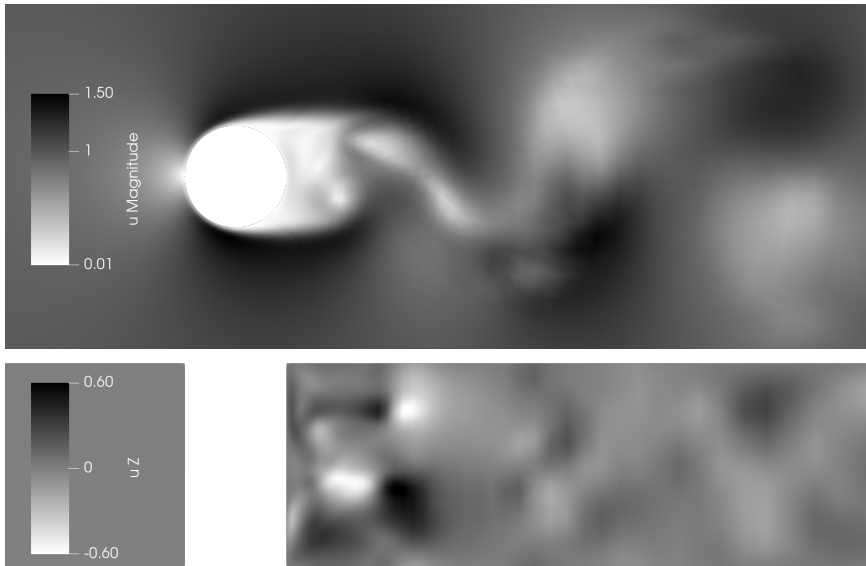


Figure 3: 2-D slices of the flow field on the finer mesh. Top: vertical cross-section, plotted by the magnitude of velocity. Bottom: horizontal cross-section, plotted by the spanwise velocity. The bottom picture shows the flow is 3-D. All velocities are normalized by the freestream velocity  $U_0 = 33.0$ .



Figure 4: Flow field on the finer mesh averaged over a time span of  $168t_0$ , plotted by the  $\rho U$  component, normalized by  $\rho_0 U_0$ .

### 3. Covariant Lyapunov Vectors (CLV) and hyperbolicity

#### 3.1. Definitions of primal and tangent solutions

Both Covariant Lyapunov Vectors (CLV) and shadowing directions are tangent solutions, which describe evolutions of trajectory perturbations caused by perturbations on a dynamical system. There are two kinds of perturbations we can perform to a dynamical system given in equation (3.1): perturbation on initial conditions and on system parameters. The corresponding tangent solutions are homogeneous and inhomogeneous tangent solutions, respectively. As we shall see, CLVs are special homogeneous tangent solutions, while shadowing directions are special inhomogeneous tangent solutions.

We write the governing equation of the flow field in the form of a general dynamical system, which will be referred as the primal system:

$$\frac{du}{dt} = f(u, s), \quad u|_{t=0} = u^0 + v^0 s + w^0 \phi. \quad (3.1)$$

Here  $f(u, s) : X \times \mathbb{R} \rightarrow X$  is a smooth function,  $u$  is state variables, and  $s$  is the system

parameter. The initial condition is  $u^0$  with a possible perturbation in the direction of  $v^0$  or  $w^0$ , controlled by  $s$  and another parameter  $\phi$ . A primal solution  $u : \mathbb{R} \rightarrow X$  maps time to a function space  $X$ , where a single point represents an entire 3-D flow field at an instant, thus  $u(t)$  can as well be imagined as a trajectory in  $X$ . For simplicity of discussions, we assume the system is autonomous, that is,  $f$  does not depend on time.

Our dynamical systems considered in this paper is given by the semi-discretized Navier-Stokes equation without turbulence models. More specifically, on the spatial direction, the flow field, together with boundary conditions, is represented by the finite-volume method on our meshes. The state variables are conservative variables, that is,  $\rho$ ,  $\rho U$ , and  $\rho E$ . Hence our function space  $X = \mathbb{R}^m$  is finite-dimensional, with  $m$  being the degrees of freedom (DOF). For the coarser mesh, the DOF is about  $1.9 \times 10^6$ ; for the finer mesh, DOF is about  $3.8 \times 10^6$ . On the other hand, we regard the temporal direction as being continuous, thus our dynamical system is continuous, and later the theories we use are for continuous dynamics.

We differentiate equation (3.1) with respect to  $\phi$ , and define  $w = du/d\phi$ , then  $w$  satisfies the so called homogeneous tangent equation:

$$\frac{dw}{dt} - \partial_u f w = 0, \quad w(t=0) = w^0, \quad (3.2)$$

where  $\partial_u f \in \mathbb{R}^{m \times m}$ , and the ODE is called the homogeneous tangent ODE.  $w$  reflects the trajectory perturbation caused by perturbing initial condition in the direction of  $w^0$ . On the other hand, if we differentiate equation (3.1) with respect to  $s$ , and define  $v = du/ds$ , then  $v$  satisfies the inhomogeneous tangent equation:

$$\frac{dv}{dt} - \partial_u f v = \partial_s f, \quad v(t=0) = v^0, \quad (3.3)$$

where  $\partial_s f \in \mathbb{R}^m$ , and the ODE is called the inhomogeneous tangent ODE.  $v$  reflects the trajectory perturbation caused by perturbing the system parameter  $s$ , which not only affects the governing differential equation, but also potentially impacts the initial condition in the direction of  $v^0$ . The solution set of an inhomogeneous tangent ODE can be written as a particular inhomogeneous  $v^*$  plus the solution set of the homogeneous tangent ODE, which is a linear subspace due to homogeneity.

### 3.2. Definitions of CLVs and hyperbolicity

A Covariant Lyapunov Vector (CLV),  $\zeta(t)$ , is a homogeneous tangent solution whose norm behaves like an exponential function of time. That is, there are  $C_1, C_2 > 0$  and  $\lambda \in \mathbb{R}$ , such that for any  $t$ ,

$$C_1 e^{\lambda t} \|\zeta(u(0))\| \leq \|\zeta(u(t))\| \leq C_2 e^{\lambda t} \|\zeta_j(u(0))\|, \quad (3.4)$$

where the norms are Euclidean norm in  $\mathbb{R}^m$ , and  $\lambda$  is defined as the Lyapunov Exponent (LE) corresponding to this CLV. CLVs with positive LEs are said to be unstable, CLVs with negative LEs are stable, and CLVs with zero LEs are neutral. For more details of LEs and CLVs, we refer readers to (Katok & Hasselblatt 1997). In this paper, we sort LEs by decreasing order, so the  $j$ -th largest LE and its corresponding CLV will be called the  $j$ -th LE and  $j$ -th CLV, respectively.

Hyperbolicity is roughly defined as that the tangent space at every state splits into stable subspace, unstable space, and neutral subspace. There are several kinds of hyperbolicity, the most widely used in ergodic theory being the uniform hyperbolicity, which further specifies that the neutral subspace is one dimensional. Our system can not be uniform hyperbolic since it has at least two neutral CLVs corresponding to the time and

spanwise translations. Less restrictive is the partial hyperbolicity, which only assumes the three subspaces are uniformly bounded away from each other.

We will first check our systems for partial hyperbolicity by checking that the angles between CLVs are large enough. More specifically, we want to bound the norm of the operator which projects to one of the subspaces, i.e. the  $C_\alpha$  given in lemma A.3 and lemma B.4 in (Ni 2018b), where we showed that  $C_\alpha = (1 - \cos^2 \alpha)^{-1/2}$ , with  $\alpha$  being the smallest angle between subspaces. Of course, the ideal case would be that these subspaces are orthogonal to each other, leading to  $\alpha = 90^\circ$  and  $C_\alpha = 1$  takes its minimum. Both the norm of shadowing direction Pilyugin (1997) and the error in FD-NILSS (Ni & Wang 2017) are proportional to  $C_\alpha$ , and we do not want it larger than 10, causing impact of an order of magnitude. The corresponding angle is  $\alpha_0 = 5.7^\circ$ , which serves as our threshold.

As we will see, although our conclusion for partial hyperbolicity is positive, the answer can be affected by technical details, and it is suspicious whether more chaotic fluid systems are as lucky. In fact, this is one reason fluid researchers are reluctant to perform Lyapunov analysis or to use tools given by ergodic theory.

However, we find a more robust form of hyperbolicity, that is, angles between two CLVs become much larger if their indexes are further apart. This hyperbolicity is weaker than partial hyperbolicity since it allows tangencies between adjacent CLVs, but it is also more robust, and has more structures. In fact, we can even visualize this weak hyperbolicity by showing that active areas of CLVs are different.

More importantly, we will show that the loss of uniform hyperbolicity is not a disaster for tools given by ergodic theories, although they mostly use uniform hyperbolicity as logical assumptions. Specifically, if we can still compute shadowing directions which correctly reflecting sensitivities of statistics of the fluid system, we will have more confidence in these methods for general chaotic systems.

### 3.3. Numerical methods for computing LEs and CLVs

The algorithm we use to compute LEs is given by Benettin *et al.* (1980), and the algorithm for CLVs is by Ginelli *et al.* (2007, 2013). Since these two algorithms share many same procedures, we describe them together. For  $i = 0, \dots, K - 1$ , we define the  $i$ -th time segment as time span  $[t_i, t_{i+1}]$ , with  $t_i = i\Delta T$ . In the algorithm presented below, for quantities defined on the entire segments such as  $u_i$  and  $W_i$ , we use the same subscript as the segment they are defined on. For quantities defined only at interfaces between segments such as  $Q_i$  and  $R_i$ , we use the same subscript as the time point they are defined at.

To start with, we should prescribe: 1) number of LEs/CLVs to compute,  $M$ ; 2) length of each time segment,  $\Delta T$ ; 3) number of time segments,  $K$ . Consequently, the time length of the entire trajectory,  $T = K\Delta T$ , is determined. Then the algorithms are given by the following procedures.

1. Generate initial conditions for primal solutions and homogeneous tangent solutions.
  - 1.1. Compute the primal solution of equation (3.1) for sufficiently long time so that the trajectory lands onto the attractor, then set  $t = 0$ , and set initial condition of the primal system,  $u_0(0)$ .
  - 1.2. Randomly generate an  $m \times M$  orthogonal matrix  $Q_0 = [q_{01}, \dots, q_{0M}]$ . This  $Q_0$  will be used as initial conditions for homogeneous tangent solutions.
2. For  $i = 0$  to  $K - 1$ , on segment  $i$ , where  $t \in [t_i, t_{i+1}]$ , do:
  - 2.1. Compute the primal solution  $u(t)$  from  $t_i$  to  $t_{i+1}$ .
  - 2.2. Compute homogeneous tangent solutions  $W_i(t) = [w_{i1}(t), \dots, w_{iM}(t)]$ .

- 2.2.1. For each homogeneous tangent solutions  $w_{ij}$ ,  $j = 1, \dots, M$ , starting from initial condition  $w_{ij}(t_i) = q_{ij}$ , integrate equation (3.2) from  $t_i$  to  $t_{i+1}$ .
- 2.2.2. Perform QR factorization:  $W_i(t_{i+1}) = Q_{i+1}R_{i+1}$ , where  $Q_{i+1} = [q_{i+1,1}, \dots, q_{i+1,M}]$ .

3. The  $j$ -th largest LE,  $\lambda_j$ , is approximated by:

$$\lambda_j = \frac{1}{K\Delta T} \sum_{i=1}^K \log |D_{ij}|, \quad (3.5)$$

where  $D_{ij}$  is the  $j$ -th diagonal element in  $R_i$ . This formula for  $\lambda_j$  converges to the true value as  $T$  becomes large.

4. We define a  $m \times M$  matrix  $V(t)$  by:

$$V(t) = W_i(t)R_{i+1}^{-1} \cdots R_K^{-1}, \quad t \in [t_i, t_{i+1}]. \quad (3.6)$$

The  $j$ -th column of  $V(t)$  converges to the direction of the  $j$ -th CLV when both  $t$  and  $(T - t)$  become large. Notice that although  $V(t)$  has different expressions on different segments, its columns are continuous across all segments.

We discuss the inner product we implicitly used in defining the orthogonality of the  $Q$  matrices. The inner product between two flow fields at a instant is a summation of inner products between different components. For consistency of units, we normalize each component by freestream properties. Moreover, we should prescribe a geometric metric for inner products between the same components. This metric should have bounded total volume, so that inner products are finite; it should also put more weight closer to the cylinder, so that FD-NILSS have better accuracy for surface objectives we use later. A natural selection of such metric is simply one where all mesh cells are equally weighted, and the entire space outside the mesh has weight zero. More specifically, with subscript  $l$  denoting different components,  $k$  denoting different cells of the mesh, for  $v, w \in X = \mathbb{R}^m$ , we define inner products as

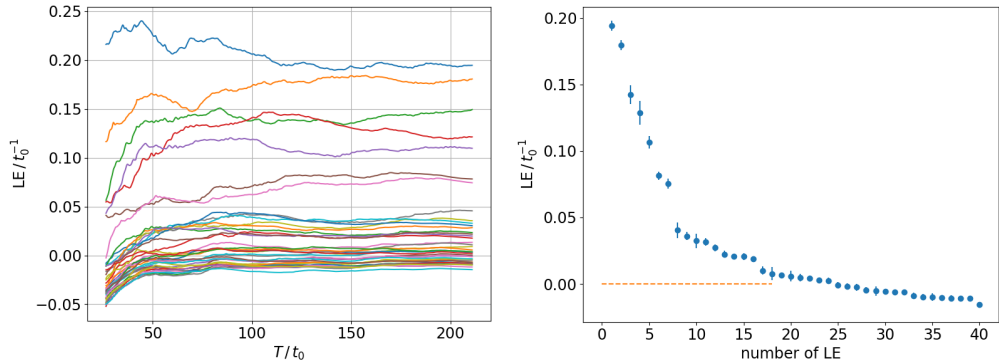
$$v^T w := \frac{1}{m'} \sum_{k=1}^{m'} v_k^T w_k, \quad \text{where} \quad v_k^T w_k := \frac{1}{3} \left( \frac{v_{k1} w_{k1}}{\rho_0^2} + \frac{\sum_{l=2}^4 v_{kl} w_{kl}}{\rho_0^2 U_0^2} + \frac{v_{k5} w_{k5}}{\rho_0^2 E_0^2} \right). \quad (3.7)$$

Here  $m'$  is the number of cells. We order the 5 components of states by  $\rho$ ,  $\rho U$ ,  $\rho E$ , and normalize all components of  $\rho U$  by  $\rho U_0$ . Under our definitions, the norm of a flow field with everywhere same to the freestream is one.

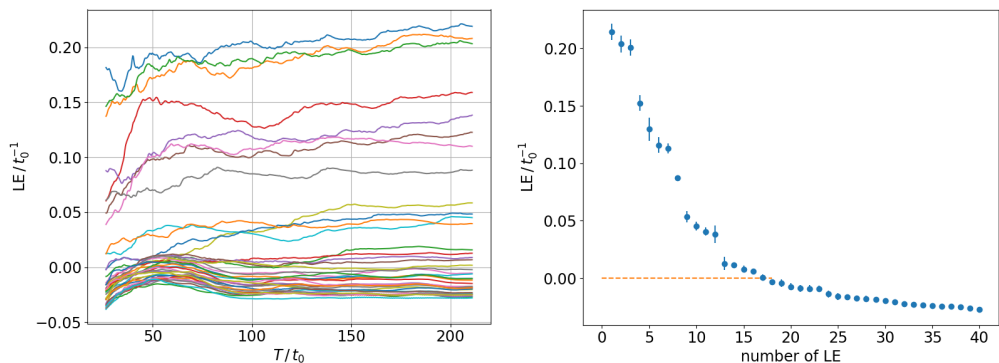
The convergence of CLV in the above algorithm is in terms of the distance between 1-dimensional subspaces. Since a CLV is a homogeneous tangent solution, we can multiply it by any factor, and still get a homogeneous tangent solution whose norm behaves like a exponential function with the same LE, which, by definition, is still the same CLV. In other words, it is only the directions of CLVs are meaningful, but not the magnitudes. Hence we can normalize CLVs by any factor we like. In this paper, we normalize CLVs such that their maximal values are 1.0.

In this paper, we use finite difference to approximate tangent solutions. To approximate a homogeneous solution  $w$  with initial condition  $w^0$ , we use the definition  $w = du/d\phi \approx \Delta u/\Delta\phi$ , where  $\phi$  controls the perturbation in the initial condition in the direction of  $w^0$ . More specifically, we compute a perturbed primal solution  $u^w$  with a perturbed initial condition  $u^0 + \Delta\phi$ , and the approximation for  $w$  is  $w \approx (u^w - u)/\Delta\phi$ , where  $u$  is the base trajectory.





(a) Results on the coarser mesh. The largest LE is  $0.20t_0^{-1}$ , meaning in one flow-through time  $t_0$ , the norm of the first CLV becomes  $e^{0.20} = 1.22$  times larger.



(b) Results on the finer mesh. The largest LE is  $0.21t_0^{-1}$ .

Figure 5: Lyapunov exponents (LE) normalized by  $t_0^{-1}$ . Left: convergence history of the first 40 different LEs. Right: confidence intervals of LEs.

### 3.4. Results of Lyapunov exponents

The time step size used for computing LEs and CLVs is the same as in the numerical simulation, that is,  $\Delta t = 10^{-8} = 1.32 \times 10^{-3}t_0$ . The number of homogeneous tangent solutions we compute is  $M = 40$ . Each segment has 200 time steps, which gives  $\Delta T = 2 \times 10^{-6} = 0.264t_0$ . The total number of time segments is  $K = 800$ , hence the time length of the entire trajectory is  $T = 1.6 \times 10^{-3} = 211t_0$ .

With above numerical settings, the convergence history of the first 40 LEs are shown in the left of figure 5. As explained in (Ni & Wang 2017), the confidence interval of a LE is estimated by the smallest interval which bounds the history of the LE and whose size shrinks as  $T^{-0.5}$ . The first 40 LEs and their confidence intervals are shown in the right of figure 5.

We can see that LE results depend on the meshes, as similarly discussed by Fernandez & Wang (2017b). In figure 5, although the general shape of the LE spectrum looks similar, but a closer look will find that the finer mesh has larger but fewer positive LEs. As a result, the selection of neutral CLVs is ambiguous and changes due to meshes.

However, we will show there are several important physical phenomena which, although they are logically consequential to the Lyapunov analysis results, but these phenomena exist robustly regardless of the detailed value of the LE spectrum. This is similar to

the chaotic hypothesis (Gallavotti 2008), which says many tools logically consequential to uniform hyperbolicity assumption are in fact valid for a larger class of dynamical systems. More specifically, those phenomena are:

1. the dimension of the attractor is much lower than the dimension of the system;
2. the system is weakly hyperbolic, as discussed in section 3.2, and in particular, CLVs are active at different locations;
3. shadowing directions exist, and reflect the linear response of statistics to parameter perturbations.

The focus of this paper will be the later two phenomena. Moreover, for engineering interests, we will show that FD-NILSS can compute shadowing directions and further the linear response with reasonable cost.

We first show that the dimension of the attractor is much lower than the dimension of the system. Intuitively, to remain its invariant hyper-volume, the attractor manifold should contain enough contracting (stable) CLVs to balance out the expansion caused by unstable CLVs. More specifically, (Frederickson *et al.* 1983) estimated the attractor dimension by to so-called Lyapunov dimension:

$$D_\lambda = N + \frac{1}{|\lambda_{N+1}|} \sum_{j=1}^{j=N} \lambda_j \in [N, N + 1], \quad (3.8)$$

where  $N$  is such that  $\lambda_1 + \lambda_2 + \dots + \lambda_N > 0$  and  $\lambda_1 + \lambda_2 + \dots + \lambda_{N+1} < 0$ . We want to give a bound to  $N$  on the finer mesh. To do this, we remind readers that the algorithm we are using computes LEs by descending order, so we have  $\lambda_j \leq \lambda_{40}$  for all  $j \geq 40$ . Using the first condition of  $N$ , we have

$$\sum_{j=1}^{40} \lambda_j + (N - 40)\lambda_{40} = \sum_{j=1}^{40} \lambda_j + \sum_{j=41}^N \lambda_{40} \geq \sum_{j=1}^{40} \lambda_j + \sum_{j=41}^N \lambda_j > 0, \quad (3.9)$$

which further leads to

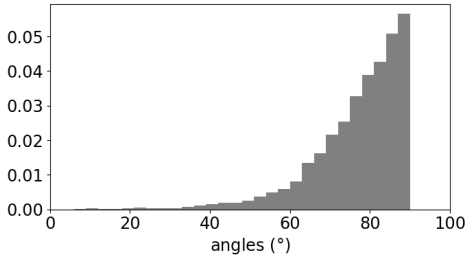
$$N \leq 40 + \frac{\sum_{j=1}^{40} \lambda_j}{|\lambda_{40}|} = 40 + \frac{1.031}{0.027} = 78. \quad (3.10)$$

On the other hand, since  $\lambda_1 + \dots + \lambda_{40} > 0$ , by the second property of  $N$ , we know  $N > 40$ . Hence the Lyapunov dimension  $41 \leq D_\lambda \leq 79$ . In other words, the chaotic dynamic of our flow problem on the finer mesh can be attributed to the interaction of fewer than 79 degrees of freedom. Using same method, we can estimate the attractor dimension on the coarser mesh is smaller than 109.

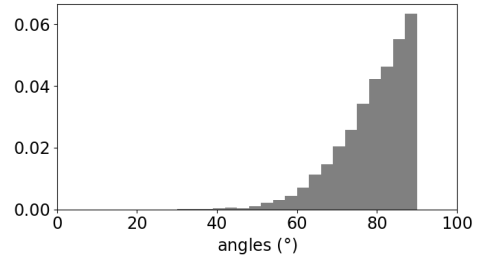
### 3.5. Results of CLVs and hyperbolicity

In the left of figure 6, we plot the histogram of angles between all pairs of the first 40 CLVs, which are perturbations whose norm grows exponentially, as defined in equation (3.4). Notice the range of angles is  $[0^\circ, 90^\circ]$ , since the angle between directions of two CLVs is the angle between subspaces of dimension one. For the finer mesh the smallest angle is  $16.4^\circ$ , passing the partial hyperbolicity test by a large margin. However, for the coarser mesh, the smallest angle is only  $5.8^\circ$ , barely larger than the threshold value, which is  $5.7^\circ$ . Small angles are rare events though, and the majority of angles are large.

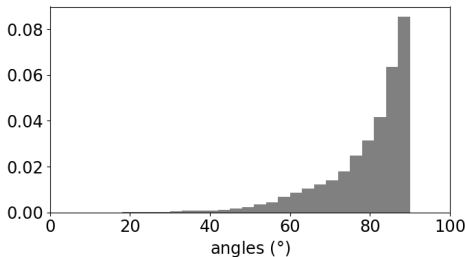
We may neglect the rare tangencies among CLVs and conclude that our fluid system is partially hyperbolic. However, the narrow pass of the test and the dependency on



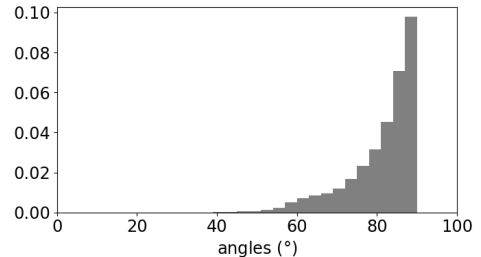
(a) Coarser mesh, all CLVs, smallest angle is  $5.8^\circ$ .



(b) Coarser mesh, CLVs indices more than 5 apart, smallest angle is  $29.2^\circ$



(c) Finer mesh, all CLVs, smallest angle is  $16.4^\circ$ .



(d) Finer mesh, CLVs indices more than 5 apart, smallest angle is  $40.8^\circ$ .

Figure 6: Histogram of angles between CLVs on segments 350 to 449, with the entire trajectory of length  $T = 211t_0$  partitioned into  $K = 800$  segments. The total area of the histogram is normalized to 1.

implementations calls for a closer examination, through which we can find either a more robust definition of hyperbolicity or some robust physical phenomena not depending on implementations.

A closer look into CLVs results finds that tangencies happen only among adjacent CLVs: this result is similar to that obtained by (Xu & Paul 2016). Hence we plot the angles between CLVs whose indices are more than 5 apart. For example, for the 20th CLV, we consider its angles with 1st to 15th CLV and 25th to 40th CLV. This result is plotted in the right of figure 6.

As we can see, when the exponents of CLVs are further apart, their angles becomes larger. So on one hand, what we observe could have been weaker than partial hyperbolicity if the occasional tangencies fail the threshold. But on the other hand, our observation is even stronger than uniform hyperbolicity, because it specifies a trend not suggested by the definition of both uniform and partial hyperbolicity. In this paper, we temporarily call this type of hyperbolicity the weak hyperbolicity.

In fact, for two CLVs whose exponents are apart, their angles are so large that we can even observe the difference in active areas. To illustrate, for the coarser mesh, we plot the 1st and 40th CLV in figure 7. For the finer mesh, we plot the 1st, 5th, 17th, and 40th CLV in figure 8. We remind readers that only the direction of CLVs, that is, only the relative flow pattern of CLVs, are meaningful. Since our primal solution lives in the function space  $X = \mathbb{R}^m$  whose tangent space is itself, for any time  $t$ , a CLV  $\zeta(t)$  lives in the same function space as the primal solution  $u(t)$ . In our 3-D flow problem, this means our CLVs also have  $\rho$ ,  $\rho U$ ,  $\rho E$  components, and we plot  $|\rho U|$ .

As we can see in both figure 7 and 8, the general trend is that the active areas of

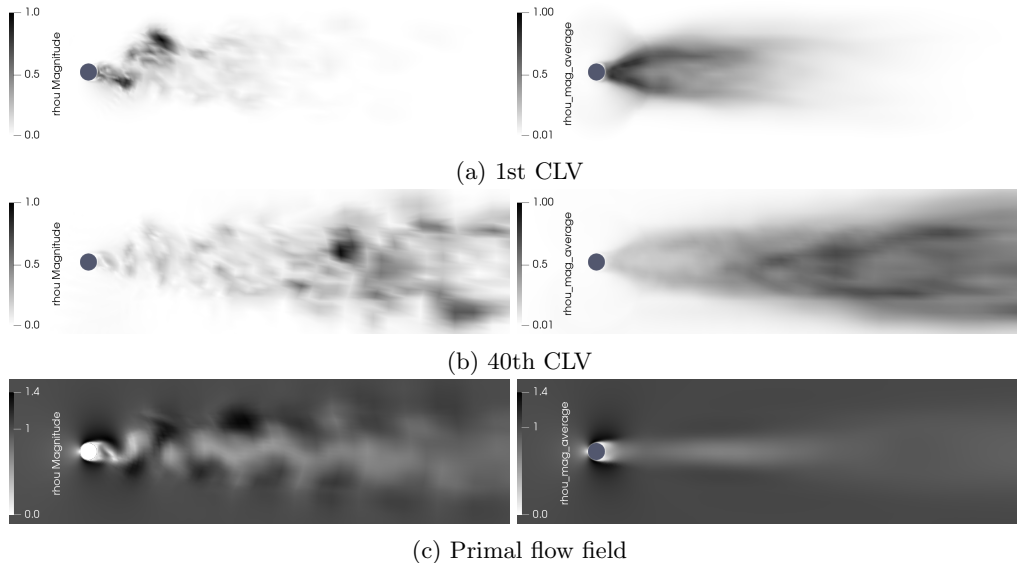


Figure 7: CLV computed on the coarser mesh on a trajectory of time length  $T = 211t_0$ . Left: snapshots at  $T/2$ . Right: averaged over time span  $[0.45T, 0.55T]$ . Plotted by the magnitude of  $\rho U$  component, and normalized such that the largest value is 1.00. The primal flow at the bottom is normalized by  $\rho_0 U_0$ .

CLVs move downstream as exponents become smaller. Intuitively, in boundary layers and near wakes, chaos is generated; perturbations in these places tend to grow, resulting in unstable CLVs. On the other hand, in far wakes, chaos is dissipated; perturbations in this region tend to decay, resulting in stable CLVs. Further, we can rationally conjecture the location of neutral CLVs is in between stable and unstable CLVs, that is, their active area is the entire wake. This conjecture is also backed by observing plot of a neutral CLV in figure 8c.

We conjecture that perturbations in the stagnant area in front of the cylinder will be dissipated, resulting in stable CLVs. This is because the fluid motion in front of the cylinder is almost determined, that is, fluid here should decelerate into a stagnancy. If we make a perturbation to this area, the fluid motion in the long term will not be changed. Hence, such a perturbation could not last long, and the corresponding LE should be negative. Our conjecture is also partly evidenced by the fact that the first 40 CLVs are not active in this area.

We further conjecture that perturbations in the freestream are also dissipated, resulting in stable CLVs. We provide two arguments supporting this conjecture. First, assume we make a perturbation in the freestream, then after changing reference frame, this is equivalent to make a small perturbation in a stagnant fluid domain; the Euclidean norm of such a perturbation decays due to the dissipation in N-S equations. Second, since our metric, induced by equation 3.7, is compactly supported, a perturbation in the freestream will be transported outside the mesh where the volume weight is zero. Hence under our norm, perturbation in the freestream decays also because the decay in the volume weight. In fact, because our norm of such perturbation decays to zero, the corresponding LE should be very negative.

To summarize, we make the following conjecture about active areas of CLVs in subsonic open flows. In subsonic open flows, unstable CLVs are active in the instability-generating

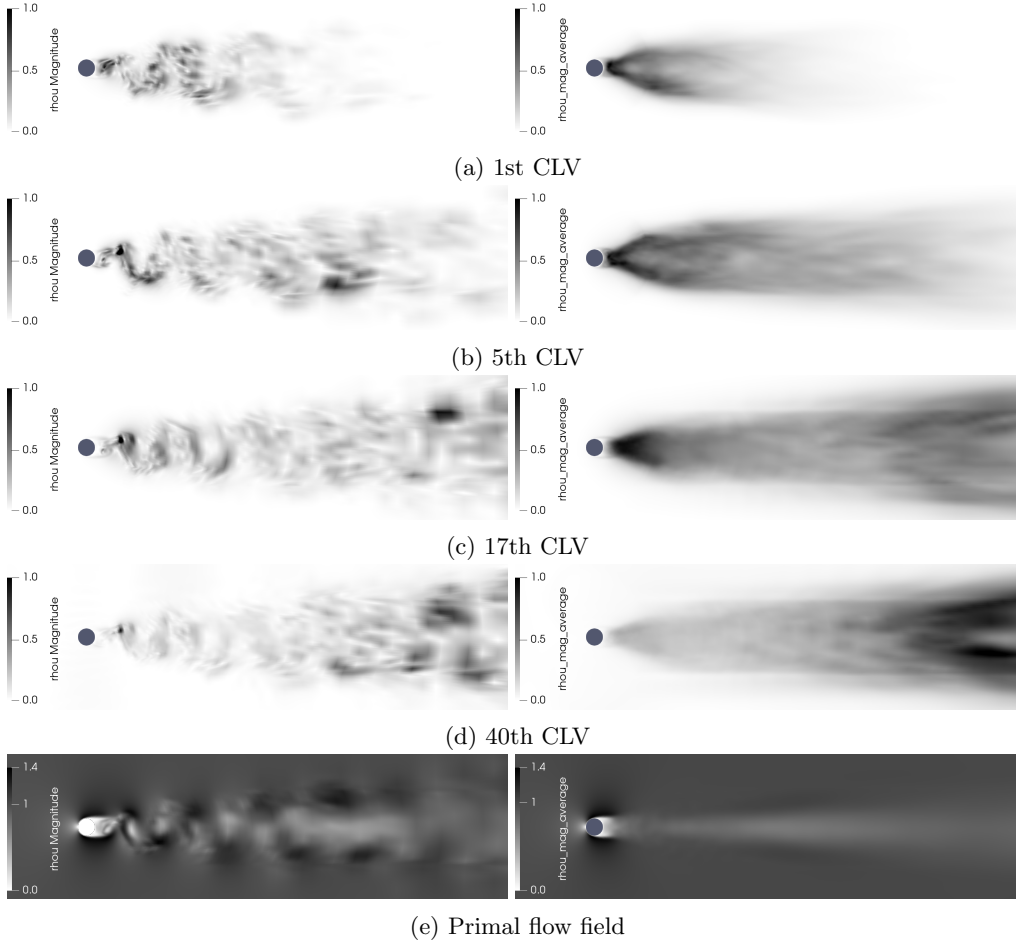


Figure 8: CLV computed on the finer mesh, using same settings as the coarser mesh.

area such as boundary layers and near wakes; the neutral CLV occupies similar locations as the wake; stable CLVs with moderately negative LEs are active in the dissipative area such as far wakes; stable CLVs active in the stagnant area ahead of the cylinder and in the freestream have very negative LEs.

To summarize, we found more structures in hyperbolicity, but our system certainly does not satisfy the uniform hyperbolicity under which shadowing methods were developed. Yet there is still hope, as the chaotic hypothesis suggested, that although the logical bridge of uniform hyperbolicity breaks down, we may find tools on the other side of bridge still useful. With this hope, we go on to examine shadowing results on our fluid system.

## 4. Shadowing directions and sensitivities

### 4.1. Definition of shadowing directions

The shadowing solution  $v^\infty$  is an inhomogeneous tangent solution whose orthogonal projection perpendicular to the trajectory,  $v^{\infty\perp}$ , is uniformly bounded on a infinitely

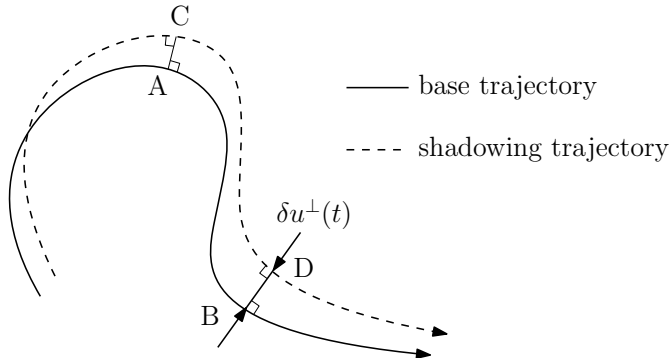


Figure 9: Shadowing directions. The base trajectory has parameter  $s$ , the shadowing trajectory has parameter  $s + \delta s$ . The first order approximation of the perpendicular distance is  $\delta u^\perp \approx v^{\infty\perp} \delta s$ . Here  $v^{\infty\perp}$  is the shadowing direction, which is an uniformly bounded inhomogeneous tangent solution.

long trajectory. Here  $\cdot^\perp$  is defined as:

$$p^\perp = p - \frac{f^T p}{f^T f} f, \quad (4.1)$$

where  $p \in \mathbb{R}^m$  is an arbitrary vector,  $f$  is the trajectory direction defined in equation (3.1), and the inner product was defined in equation (3.7). We remark here that for continuous dynamical system, the definition of shadowing direction involves a reparametrization of time (Pilyugin 1999, Definition 1.26), or equivalently a ‘time dilation’ (Wang *et al.* 2014), or projecting the tangent solutions to the subspace perpendicular to  $f$  (Ni & Wang 2017). The  $v^{\infty\perp}$  is the projection of  $v^\infty$  given by the third approach, and  $v^{\infty\perp}$  is bounded, but  $v^\infty$  is not. For convenience, we also call  $v^\perp$  the shadowing direction.

The shadowing direction has the following physical meaning. The definition of inhomogeneous tangent solution  $v = du/ds$  tells us that with perturbed parameter  $s + \delta s$ , there is a new trajectory  $u + \delta u$  such that  $\delta u \approx v^\infty \delta s$ . Now the perpendicular distance between the new and the old trajectory is  $\delta u^\perp \approx v^{\infty\perp} \delta s$ , together with the boundedness of  $v^{\infty\perp}$ , we see that the new trajectory remains perpendicularly close to the old trajectory for a long time. This new trajectory will be referred as the shadowing trajectory, and the old as the base trajectory. This intuition of the shadowing direction is shown in figure 9.

The initial condition of the shadowing direction is not known apriori, or equivalently, we do not specify how system parameters would affect initial conditions. In fact, as we shall see, although the shadowing direction solves that same ODE as in equation (3.3), its determining condition is no longer the initial condition; rather, to determine a shadowing direction, we minimize the  $L^2$  norm of the orthogonal projection of an inhomogeneous tangent solution.

#### 4.2. Sensitivity analysis of long-time averages via shadowing directions

For chaotic dynamical systems such as the 3-D flow problem in this paper, the output of the system, such as the drag or lift, is typically aperiodic. As often happens in engineering, the objective is the long-time average  $\langle J \rangle_\infty$  of an instantaneous quantity  $J(u, s) : \mathbb{R}^m \times \mathbb{R} \rightarrow \mathbb{R}$ . More specifically, we define:

$$\langle J \rangle_\infty := \lim_{T \rightarrow \infty} \langle J \rangle_T, \quad \text{where } \langle J \rangle_T := \frac{1}{T} \int_0^T J(u, s) dt. \quad (4.2)$$

$\langle J \rangle_\infty$  is usually approximated by a  $\langle J \rangle_T$  with a large  $T$ . The sensitivity of the objective with respect to system parameters,  $d\langle J \rangle_\infty/ds$ , is of engineering interest. In this subsection we show how to compute the sensitivity using the shadowing direction.

Assume we have found, on a finitely long trajectory, an approximation  $v \approx v^\infty$ , where  $v$  is also an inhomogeneous tangent solution. We first define the time dilation term (Wang *et al.* 2014)  $\eta$ :

$$\frac{dv^\perp}{dt} = \partial_u f v^\perp + \partial_s f + \eta f. \quad (4.3)$$

Intuitively,  $\eta$  describes the relative time spent on the shadowing trajectory in comparison with the base trajectory. In figure 9, if the shadowing trajectory takes less time to travel from point C to D than the base trajectory from A to B, then equation (4.3) gives  $\eta < 0$ . On the other hand, if the shadowing trajectory moves slower, then  $\eta > 0$ .

Once we get  $v$  and  $\eta$ , the sensitivity can be computed by:

$$\frac{d\langle J \rangle_\infty}{ds} \approx \frac{1}{T} \int_0^T [\partial_u J v^\perp + \partial_s J + \eta(J - \langle J \rangle_T)] dt, \quad (4.4)$$

where  $\langle J \rangle_T$  is defined in equation (4.2). Intuitively, the first term inside the integration in equation (4.4) describes the contribution by the perpendicular distance between the shadowing trajectory and the base trajectory. The second term is due to the fact the function  $J$  may explicitly depend on  $s$ . The last term involves  $\eta$ , and it accounts for the fact that the average is taken with respect to time: if in some small region the shadowing trajectory moves faster than the base trajectory, then the time spent is shorter, hence the contribution from this region in the time average should also be smaller.

Another formula for the sensitivity is easier for computer programming:

$$\frac{d\langle J \rangle_\infty}{ds} \approx \frac{1}{T} \left[ \int_0^T (\partial_u J v + \partial_s J) dt + \xi|_0^T \langle J \rangle_T - (\xi J)|_0^T \right], \quad (4.5)$$

where the time difference term,  $\xi$ , is a time-dependent scalar function such that:

$$\xi f = v - v^\perp. \quad (4.6)$$

$\xi$  is easier to compute than  $\eta$ , since its definition does not involve time derivative. Notice that in equation (4.5), we use  $v$  instead of its projection  $v^\perp$ . The derivation of equation (4.4), equation (4.5), and their relation can be found in the appendix of (Ni & Wang 2017).

### 4.3. The NILSS algorithm for computing shadowing directions

We describe the Non-Intrusive Least Squares Shadowing (NILSS) algorithm in this subsection. Same as in section 3.3, for  $i = 0, \dots, K - 1$ , we define the  $i$ -th time segment as  $[t_i, t_{i+1}]$ , with  $t_i = i\Delta T$ . In the algorithm presented below, for quantities defined on the entire segments, such as  $u_i, W_i, v_i^*, C_i$ , and  $d_i$ , we use the same subscripts as the segments they are defined on. For quantities defined only at interfaces between segments, such as  $Q_i, R_i$ , and  $b_i$ , we use the same subscripts as the time points they are defined at. Again, we use finite difference results to approximate tangent solutions: such variant is called the Finite Difference Non-Intrusive Least Squares Shadowing (FD-NILSS) algorithm, whose details are given in (Ni *et al.* 2018).

To start with, we should prescribe: 1) number of homogeneous tangent solutions,  $M$ , which must be larger than the number of unstable CLVs,  $m_{us}$ ; 2) length of each time segment,  $\Delta T$ ; 3) number of time segments,  $K$ . Consequently, the time length of the

entire trajectory,  $T = K\Delta T$  is also determined. Then, the NILSS algorithm is given by the following procedures.

1. Generate initial conditions for primal solutions, homogeneous tangent solutions, and inhomogeneous tangent solutions.

1.1. Compute the primal solution of equation (3.1) for sufficiently long time so that the trajectory lands onto the attractor, then set  $t = 0$ , and set initial condition of the primal system,  $u_0(0)$ .

1.2. Randomly generate an  $m \times M$  orthogonal matrix  $Q_0 = [q_{01}, \dots, q_{0M}]$  whose column vectors are orthogonal to  $f(t = 0)$ . This  $Q_0$  will be used as initial conditions for homogeneous tangent solutions.

1.3. Set initial condition of the particular inhomogeneous tangent solution  $v_0^*(0) = 0$ .

2. For  $i = 0$  to  $K - 1$ , on segment  $i$ , where  $t \in [t_i, t_{i+1}]$ , do:

2.1. Compute the primal solution  $u_i(t)$  from  $t_i$  to  $t_{i+1}$ .

2.2. Compute homogeneous tangent solutions  $W_i(t) = [w_{i1}(t), \dots, w_{iM}(t)]$ .

2.2.1. For each homogeneous tangent solutions  $w_{ij}$ ,  $j = 1, \dots, M$ , starting from initial condition  $w_{ij}(t_i) = q_{ij}$ , integrate equation (3.2) from  $t_i$  to  $t_{i+1}$ .

2.2.2. Compute orthogonal projection  $W_i^\perp(t) = [w_{i1}^\perp(t), \dots, w_{iM}^\perp(t)]$  via equation (4.1).

2.2.3. Compute and store the covariant matrix on segment  $i$ :

$$C_i = \int_{t_i}^{t_{i+1}} (W_i^\perp)^T W_i^\perp dt. \quad (4.7)$$

2.2.4. Perform QR factorization:  $W_i^\perp(t_{i+1}) = Q_{i+1} R_{i+1}$ , where  $Q_{i+1} = [q_{i+1,1}, \dots, q_{i+1,M}]$ .

2.3. compute the particular inhomogeneous tangent solution  $v_i^*(t)$ .

2.3.1. Starting from initial condition  $v_i^*(t_i)$ , integrate the inhomogeneous equation (3.3) from  $t_i$  to  $t_{i+1}$ .

2.3.2. Compute the orthogonal projection  $v_i^{*\perp}(t)$  via equation (4.1).

2.3.3. Compute and store

$$d_i = \int_{t_i}^{t_{i+1}} W_i^{\perp T} v_i^{*\perp} dt. \quad (4.8)$$

2.3.4. Orthogonalize  $v_i^{*\perp}(t_{i+1})$  with respect to  $W_{i+1}^\perp(t_{i+1}) = Q_{i+1}$  to obtain the initial condition of the next time segment:

$$v_{i+1}^*(t_{i+1}) = v_i^{*\perp}(t_{i+1}) - Q_{i+1} b_{i+1}, \quad (4.9)$$

Compute and store:

$$b_{i+1} = Q_{i+1}^T v_i^{*\perp}(t_{i+1}). \quad (4.10)$$

3. Solve the NILSS problem:

$$\min_{\{a_i\}} \sum_{i=0}^{K-1} \frac{1}{2} a_i^T C_i a_i + d_i^T a_i \quad (4.11)$$

$$\text{s.t. } a_i = R_i a_{i-1} + b_i \quad i = 1, \dots, K - 1.$$

This is a least-squares problem with arguments  $\{a_i\}_{i=0}^{K-1}$ , where  $a_i \in \mathbb{R}^M$  for each  $i$ .



4. Compute  $v_i$  within each time segment  $t \in [t_i, t_{i+1}]$ :

$$v_i(t) = v_i^*(t) + W_i(t)a_i. \quad (4.12)$$

The orthogonal projections of  $v_i$  on each segment,  $\{v_i^\perp\}_{i=0}^{K-1}$ , converges to the orthogonal projection of the shadowing direction,  $v^{\infty\perp}$ , as both  $t$  and  $T - t$  become large.

5. Compute  $\xi_i$  at the end of each segment:

$$\xi_i(t_{i+1}) = \frac{(v_i(t_{i+1}))^T f(u(t_{i+1}))}{f(u(t_{i+1}))^T f(u(t_{i+1}))}. \quad (4.13)$$

6. The derivative can be computed by:

$$\frac{d\langle J \rangle_\infty}{ds} \approx \frac{1}{T} \sum_{i=0}^{K-1} \left[ \int_{t_i}^{t_{i+1}} (\partial_u J v_i + \partial_s J) dt + \xi_i(t_{i+1})(\langle J \rangle_T - J(t_{i+1})) \right]. \quad (4.14)$$

We notice readers that although at the beginning of each segment,  $v_i$  is perpendicular to  $f(t_i)$ , typically  $v_i$  is not perpendicular to  $f(t_i)$  for the rest of the segment. In NILSS, we typically use perpendicularly projected vectors, such as  $v_i^{*\perp}, W_i^\perp, v_i^\perp$ , for constructing the minimization problem in equation (4.11) to compute the shadowing directions. Unprojected vectors, such as  $v_i$ , are typically used for computing sensitivities by equation (4.14). As shown in the appendix of (Ni & Wang 2017), we can construct a continuous  $v$ , and its orthogonal projection  $v^\perp$  confined on each segment yields  $v_i^\perp$ . However,  $v_i$  are not confinement of  $v$ , and  $v_i$  are not necessarily continuous across segments. In fact, in equation (4.11), the minimization is minimizing  $\|v^\perp\|_{L^2}$ , while constraint prescribes that  $v^\perp$  is continuous across all time segments.

Intuitively, at  $t = 0$ , the difference between  $v^{\infty\perp}$  and  $v^\perp$  contains unstable CLVs; since  $v^{\infty\perp}$  is bounded, as time evolves, the exponential growth of unstable CLVs increases both  $\|v^{\infty\perp} - v^\perp\|_{L^2}$  and  $\|v^{*\perp}\|_{L^2}$ . Also as time evolves the span of  $M$  homogeneous tangent solutions approximates the span of the first  $M$  CLVs, hence  $v^\perp = v^{*\perp} + W^\perp a$  allows us to subtract unstable CLVs from  $v^\perp$ . Now minimizing  $\|v^\perp\|_{L^2}$  removes unstable CLVs from both  $v^\perp$  and  $v^{\infty\perp} - v^\perp$ , thus making  $v_i^\perp \approx v^{\infty\perp}$ . Since the number of unstable CLVs is typically much smaller than the dimension of the dynamical system, NILSS is computationally efficient. The more detailed explanation of NILSS is in (Ni & Wang 2017).

#### 4.4. Results of shadowing directions

This subsection discusses the shadowing directions computed by the FD-NILSS algorithm. We remind readers that shadowing solutions depend only on choice of system parameters but not on objectives. In particular, this subsection shows two shadowing solutions with respect to two system parameters: 1) freestream velocity  $U$ , normalized by  $U_0$ ; 2) rotation speed of the cylinder  $\omega$ , measured in cycles per time unit, normalized by  $\omega_0$ .

In FD-NILSS we set time step size  $1 \times 10^{-8}$ , and 200 steps in each time segment, hence the segment length is  $\Delta T = 2 \times 10^{-6} = 0.259t_0$ : these are the same as what we used for computing LEs and CLVs. Different from those used for computing LEs and CLVs, we set the number of homogeneous tangent  $M = 30$  and the number of segments  $K = 600$ , hence the time length of the entire trajectory is  $T = 1.2 \times 10^{-3} = 158.4t_0$

We first plot the norm of shadowing directions on the finer mesh in figure 10, where the norm is induced by the inner product defined in equation (3.7). Since  $v^\perp = du^\perp/ds$ , with  $du^\perp$  already normalized by freestream constants in the definition of inner product,

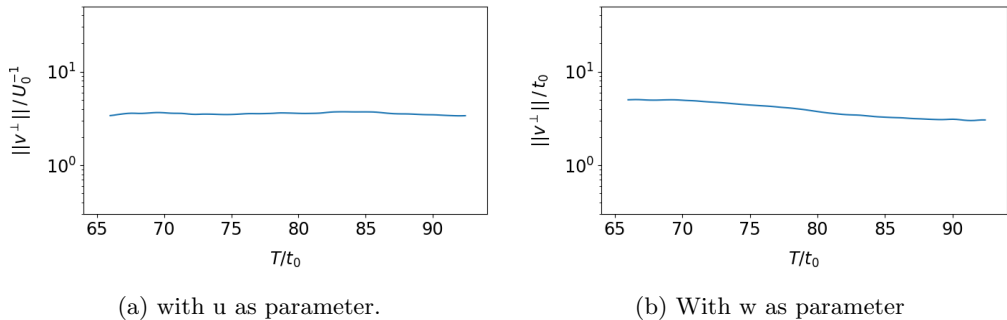


Figure 10: Norms of shadowing directions on the finer mesh, measured from  $66t_0$  to  $93t_0$ , computed on a trajectory of length  $T = 158t_0$ .

we further need to normalize shadowing directions by  $s_0^{-1}$ . Here  $s_0$  is the unit parameter, that is,  $U_0$  or  $\omega_0$ .

By observing figure 10 we can verify the uniform boundedness of shadowing directions, as the both  $\|v^\perp\|$  does not change much from from  $66t_0$  to  $93t_0$ . For comparison we may think of the first CLV, whose norm would grow  $e^{0.21 \times (93-66)} = 290$  times larger within the same time span.

Orthogonal projections of shadowing directions,  $v^\perp$ , are plotted in figure 11. Same as CLVs, for any time  $t$ ,  $v^\perp(t)$  lives in the same function space as the primal solution  $u(t)$ , hence  $v^\perp$  also has  $\rho$ ,  $\rho U$ ,  $\rho E$  components. In figure 11, for each parameter, we plot the  $|\rho U|$  field of  $v^\perp(t)$ . Unlike CLVs, both directions and magnitudes of shadowing directions are meaningful, since shadowing directions reflect not only in what direction flow fields will change due to perturbations in system parameters  $s$ , but also how large the change will be. hence, we normalize shadowing directions by freestream constants and unit parameters to preserve information of magnitudes.

If we perturb system parameters by  $\Delta U$ , the shadowing solution is a flow field with freestream property  $\rho_0(U_0 + \Delta U)$ . Since  $v^\perp$  points from the base solution to the shadowing solution, we expect the freestream area of  $v^\perp$  to be  $\rho_0 \Delta U / \Delta U = \rho_0$ . Above intuition is verified in the left of figure 11a: with  $U$  as the system parameter, the freestream area of the  $\rho U$  component of the shadowing direction  $v^\perp$  has magnitude 1, since we are normalizing by  $\rho_0$ . On the other hand, perturbing rotation speed  $\omega$  should have little effect on the freestream area: this is also verified in figure 11b, where  $v^\perp$  has small magnitude in the freestream area.

We observe by comparing left of figure 11a and figure 11b that, in the wake area, both  $v^\perp$  have similar magnitude. This fact is further confirmed by that in figure 10 both  $\|v^\perp\|$  are similarly large after normalization. This fits our intuition that, if we perturb cylinder rotation by  $\Delta\omega = 0.01\omega_0$ , then the circumferential speed is changed by  $0.01\omega_0 D/2 = 0.01U_0/2$ : this extra rotation should have similar magnitude of impact on the wake as changing the freestream velocity by  $\Delta U = 0.01U_0$ .

We compare the shadowing directions with the primal flow field in figure 11. On one hand, shadowing directions are correlated to the primal flow field, since the peak values of shadowing directions are typically located close to the vortices, indicating that vortices structures are the most sensitive to parameter perturbations.

On the other hand, because shadowing directions are perturbations, they are very different from the primal flow. The primal flow has several structures that are insensible to parameter perturbations, whereas parameter perturbations may bring new structures

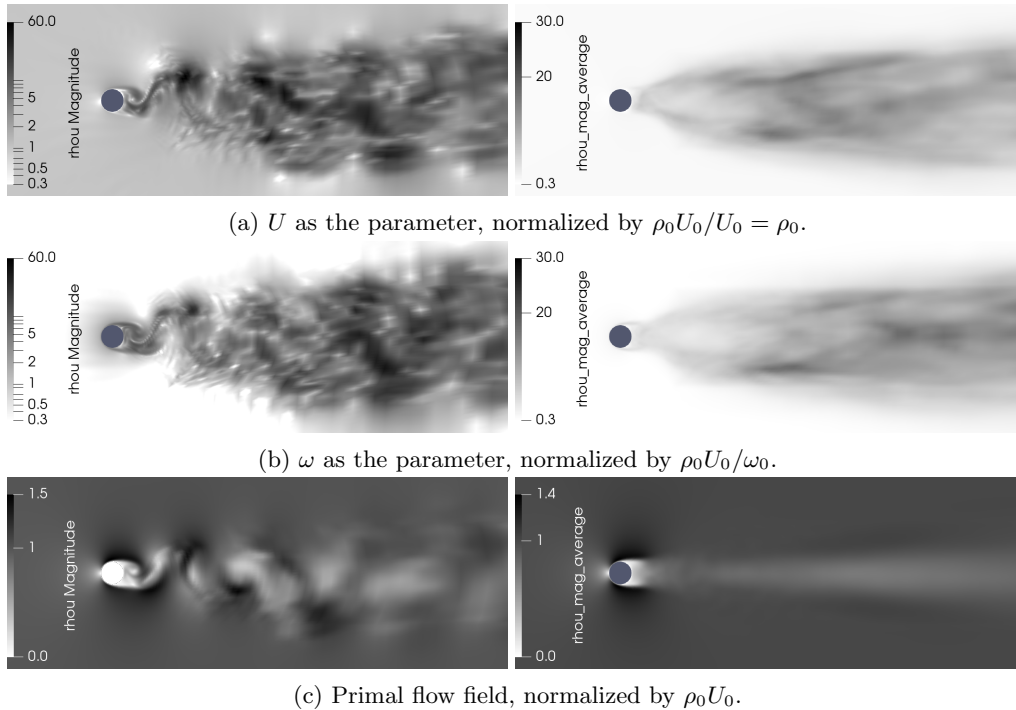


Figure 11: Magnitude of the  $\rho U$  component of the shadowing direction  $v^\perp = du^\perp / ds$  on the finer mesh, which is computed by FD-NILSS on a trajectory of time length  $T = 158t_0$ . Left: a snapshot at  $0.5T$ , colored by log scale; right: averaged from  $66t_0$  to  $93t_0$ , colored by linear scale.

to the primal flow. For example, when  $\omega$  is parameter, the stagnant area in front of the cylinder in primal flow changes to a smooth halo around the cylinder in the shadowing directions, due to the fact that perturbing  $\omega$  leads to a uniform acceleration around the cylinder. Moreover, the shadowing directions has a larger active area than the primal flow. An extreme example is the left of figure 11a, where the entire freestream of shadowing directions has value one, as we discussed. Indeed, the convolution formula of shadowing directions shows that shadowing directions are affected by both stable and unstable CLVs (Ni 2018b), the union of whose active areas cover the entire flow field.

#### 4.5. Results of sensitivities

With shadowing directions, we can compute sensitivities of long-time averaged objectives from equation (4.13) and equation (4.14) with little extra cost. In fact, as we shall see, using only a trajectory of time length  $106t_0$  should be enough to compute accurate sensitivities. In this subsection, we investigate the effect of  $U$  on the averaged drag force  $\langle D_r \rangle$ . We will normalize  $\langle D_r \rangle$  by  $F_0 = 0.5\rho U_0^2 DZ = 8.031 \times 10^{-5}$ . The objective for system parameter  $\omega$  is averaged lift  $\langle L \rangle$ , which is also normalized by  $F_0$ .

We plot the history of the sensitivities computed via shadowing directions in figure 12. For each  $T$ , we run NILSS from the same initial condition of primal and tangent solutions to  $T$ , solve the shadowing direction, using which we compute the sensitivity corresponding to  $T$ . The uncertainty of the final sensitivity is estimated by the smallest interval which bounds the history of the sensitivity and whose size shrinks as  $T^{-0.5}$ . We can see that for both meshes the uncertainty of sensitivities is below 10%.

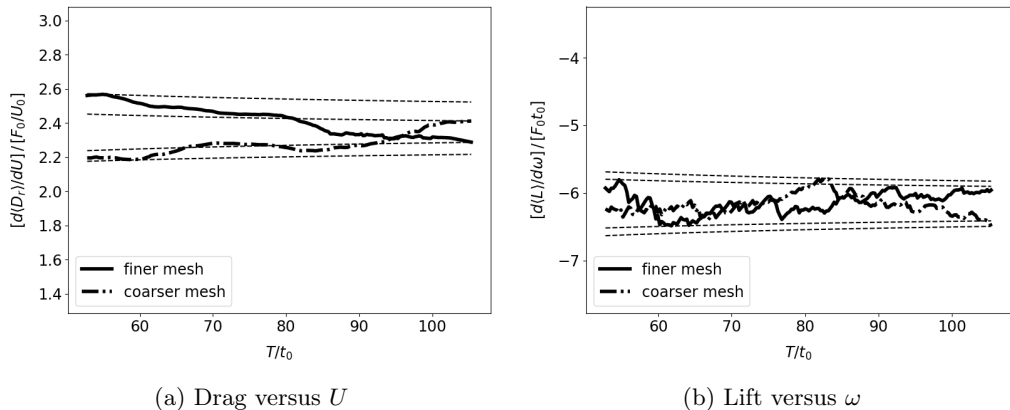


Figure 12: History plots of sensitivities computed by FD-NILSS.

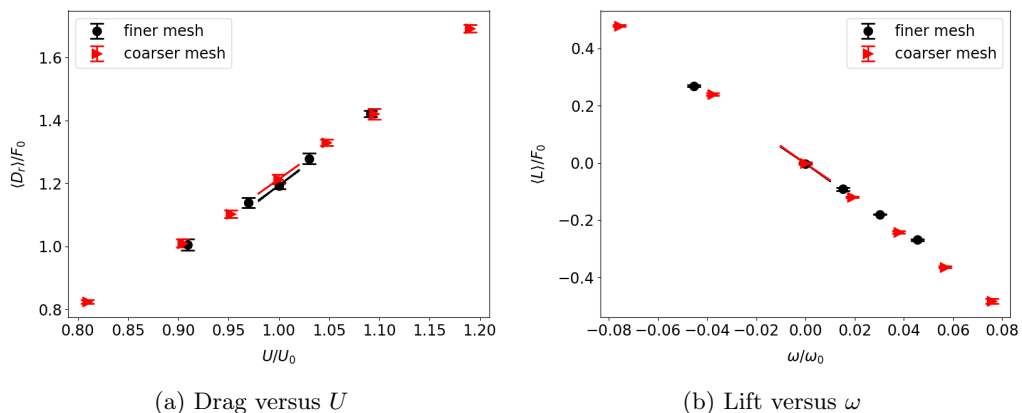


Figure 13: Sensitivities for different choices of parameters and objectives. Vertical bars indicate 95% confidence intervals of the averaged objectives. The straight lines through the middle data points indicate the sensitivities computed by FD-NILSS.

We explain how to compute uncertainty of long-time averaged objectives, which is approximated by  $\langle J \rangle_{T'}$ , the averaged instantaneous objective over  $T' = 7.68 \times 10^{-3} = 1014t_0$ . To get the uncertainty due to taking the average over finite time, we divide the history of  $J(t)$  into 5 equally long parts. Denote the objectives averaged over each of the five parts by  $J_1, \dots, J_5$ , whose corrected sample standard deviation is denoted by  $\sigma'$ . We assume that the standard deviation of  $\langle J \rangle_{T'}$  is proportional to  $T'^{-0.5}$ , so we use  $\sigma = \sigma'/\sqrt{5}$  as the standard deviation of  $\langle J \rangle_{T'}$ . We further assume  $\pm 2\sigma$  yields the 95% confidence interval, which is indicated by the vertical bar in figure 13.

The sensitivities computed via shadowing directions are shown in figure 13. For both meshes our sensitivities correctly reflect the trend between averaged-objectives and system parameters. This confirms the physical meaning of the shadowing direction: it reveals the sensitivity of all physical phenomena in this flow field with respect to perturbations in parameters, in such a way that the average of the sensitivity is the sensitivity of the average.

The cost of FD-NILSS for computing a sensitivity is mainly in integrating the primal solution over  $400 \times 200 \times 32 = 2.6 \times 10^6$  time steps. Here 400 is the number of segments,

200 is the number of time steps in each segment. 32 is the number of primal solutions computed: in FD-NILSS we need one inhomogeneous tangent and 30 homogeneous tangent solutions, and each tangent solution is approximated by the difference between a perturbed solution and the same base solution: those are 32 primal solutions in total. On the other hand, a sensitivity can be revealed by some regression among the 5 pairs of objectives and parameters in figure 13, the total cost of which is  $3.8 \times 10^6$  steps of primal simulation: this cost is similar as that of FD-NILSS. Additionally, as discussed in (Ni & Wang 2017; Ni *et al.* 2018), FD-NILSS and NILSS has smaller marginal cost for new parameters. Also, when we have a tangent solver, NILSS can be further accelerated by exploiting the fact that all tangent equations use the same Jacobian matrices. Finally, for cases with more parameters than objectives or cases when we have only adjoint solvers, the Non-Intrusive Least Squares Adjoint Shadowing (NILSAS) method (Ni 2018a) can be a good choice.

As we can see, although our system barely passes the partial hyperbolicity test, the sensitivities compute by shadowing methods seem to be robust and not affected by numerical details. We thus add one more evidence to the chaotic hypothesis, that is, although shadowing methods are logically consequential to uniform hyperbolicity, they are still valid for our fluid system, which is weak hyperbolic, barely partial hyperbolic, and certainly not uniform hyperbolic.

## 5. Conclusions

In this paper, we first compute the Lyapunov Exponents (LE) of a 3-D chaotic flow past a cylinder at Reynolds number 525. Our computation shows this flow problem has less than 30 positive LEs, but the detailed LE spectrum depends on meshes. For both meshes, we find the Lyapunov dimension is smaller than 109, meaning that the apparent complicated dynamics of our 3-D flow problem can be attributed to the interaction among less than 109 degrees of freedom.

We then compute the first 40 Covariant Lyapunov Vectors (CLV) of this 3-D flow problem. The partially hyperbolic assumption is also not violated by computing angles between CLVs, although our system on the coarser mesh passes the test by only a tiny margin, indicating this test is not robust to numerical implementations. However, we conjecture that there is a more robust form of hyperbolicity, which we temporarily name as the weak hyperbolicity, that is, the angles between CLVs get large when the exponents become further apart, although there may be occasional tangencies between adjacent CLVs. Our conjecture is backed by observing plots of CLVs, where we find that unstable CLVs are active in the instability generating area such as boundary layers and near wakes, while stable CLVs are active in more dissipative area such as far wake, front of cylinder, and the freestream. This difference in active areas is robust to meshes, and it indicates CLVs point to different directions.

We then use the Finite Difference Non-Intrusive Least Squares Shadowing (FD-NILSS) algorithm to compute the shadowing direction  $v^\perp$  of this 3-D flow problem. The magnitude of the computed  $v^\perp$  remains on the same level as time evolves, thus indicating the existence of shadowing directions of this weakly hyperbolic 3-D flow problem. By observing  $v^\perp$ , we find its freestream area is proportional to perturbations on the freestream flow speed  $U$ , but not affected by perturbations on the cylinder rotation  $\omega$ . On the other hand,  $v^\perp$  have similar magnitudes for unit perturbations on  $U$  and  $\omega$ .

Finally, we use shadowing directions to compute sensitivities of some long-time averaged objectives. For both meshes, the computed sensitivities correctly reflects the trend between system parameters and objectives. Our results confirms the physical meaning of

the shadowing solution in revealing sensitivities of all physical phenomena in this flow field with respect to perturbations on a parameter. The sensitivity results also suggest that shadowing methods are robust to numerical implementations, and are still valid for this weakly hyperbolic fluid system, although shadowing theories typically assume uniform hyperbolicity.

Possible future works involves performing similar analysis to other turbulent flow problems, to verify 1) our conjectures about weak hyperbolicity, and active areas of CLVs in open flows; 2) whether shadowing methods are still valid. Numerically, it is also of interest to further accelerate the NILSS algorithms.

## References

### REFERENCES

- ALBERS, D. J. & SPROTT, J. C. 2006 Structural stability and hyperbolicity violation in high-dimensional dynamical systems. *Nonlinearity* **19** (8), 1801–1847, arXiv: 0408011.
- BECKER, ROLAND & RANNACHER, ROLF 2001 An optimal control approach to a posteriori error estimation in finite element methods. *Acta Numerica* **10**.
- BENETTIN, GIANCARLO, GALGANI, LUIGI, GIORGILLI, ANTONIO & STRELCYN, JEAN-MARIE 1980 Lyapunov Characteristic Exponents for smooth dynamical systems and for hamiltonian systems; A method for computing all of them. Part 2: Numerical application. *Meccanica* **15** (1), 21–30.
- BEWLEY, THOMAS R. 2001 Flow control: New challenges for a new Renaissance. *Progress in Aerospace Sciences* **37** (1), 21–58.
- BLONIGAN, PATRICK J 2017 Adjoint sensitivity analysis of chaotic dynamical systems with non-intrusive least squares shadowing. *Journal of Computational Physics* **348**, 803–826.
- BLONIGAN, PATRICK J., FERNANDEZ, PABLO, MURMAN, S.M. M., WANG, QIQI, RIGAS, G. & MAGRI, L. 2016a Towards a chaotic adjoint for LES. *Center for Turbulence Research, Summer Program* pp. 385–394.
- BLONIGAN, PATRICK J, WANG, QIQI, NIELSEN, ERIC J & DISKIN, BORIS 2016b Least Squares Shadowing Sensitivity Analysis of Chaotic Flow around a Two-Dimensional Airfoil. In *54th AIAA Aerospace Sciences Meeting*, pp. 1–28.
- BOWEN, RUFUS 1970 Markov Partitions for Axiom A Diffeomorphisms. *American Journal of Mathematics* **92** (3), 725–747.
- BRÈS, GUILLAUME A, HAM, FRANK E, NICHOLS, JOSEPH W & LELE, SANJIVA K 2017 Unstructured Large-Eddy Simulations of Supersonic Jets. *AIAA Journal* **55** (4), 1164–1184.
- CHORIN, ALEXANDRE J., HALD, OLE H. & KUPFERMAN, RAZ 2002 Optimal prediction with memory. *Physica D: Nonlinear Phenomena* **166** (3-4), 239–257, arXiv: 0101022.
- COLONIUS, TIM, LELE, SANJIVA K & MOIN, PARVIZ 1993 Boundary conditions for direct computation of aerodynamic Sound Generation. *AIAA Journal* **31** (9), 1574–1582.
- FERNANDEZ, PABLO & WANG, QIQI 2017a Lyapunov spectrum of chaotic flow simulations. Application to chaotic adjoints. In *23rd AIAA Computational Fluid Dynamics Conference, Denver, CO*.
- FERNANDEZ, P. & WANG, Q. 2017b Lyapunov spectrum of the separated flow around the NACA 0012 airfoil and its dependence on numerical discretization. *Journal of Computational Physics* **350**, 453–469, arXiv: 1612.07409.
- FIDKOWSKI, KRZYSZTOF J & DARMOFAL, DAVID L 2011 Review of Output-Based Error Estimation and Mesh Adaptation in Computational Fluid Dynamics. *AIAA Journal* **49** (4), 673–694.
- FREDERICKSON, PAUL, KAPLAN, JAMES L., YORKE, ELLEN D. & YORKE, JAMES A. 1983 The liapunov dimension of strange attractors. *Journal of Differential Equations* **49** (2), 185–207.

- GALLAVOTTI, GIOVANNI 2006 Entropy, thermostats, and chaotic hypothesis. *Chaos* **16** (4), arXiv: 0606690.
- GALLAVOTTI, G 2008 Chaotic Hypothesis. *Scholarpedia* *3*(1):5906 **3** (1), 8–11.
- GALLAVOTTI, G. & COHEN, E. G D 1995 Dynamical ensembles in stationary states. *Journal of Statistical Physics* **80** (5-6), 931–970, arXiv: 9501015.
- GILES, MICHAEL B. & SÜLI, ENDRE 2002 Adjoint methods for PDEs: a posteriori error analysis and postprocessing by duality. *Acta Numerica* **11**.
- GINELLI, FRANCESCO, CHATÉ, HUGUES, LIVI, ROBERTO & POLITI, ANTONIO 2013 Covariant Lyapunov vectors. *Journal of Physics A: Mathematical and Theoretical* **46** (25), 254005, arXiv: arXiv:1212.3961v1.
- GINELLI, F., POGGI, P., TURCHI, A., CHATÉ, H., LIVI, R. & POLITI, A. 2007 Characterizing dynamics with covariant lyapunov vectors. *Physical Review Letters* **99** (13), 1–4, arXiv: 0706.0510.
- INUBUSHI, MASANOBU, KOBAYASHI, MIKI U., TAKEHIRO, SHIN ICHI & YAMADA, MICHIO 2012 Covariant lyapunov analysis of chaotic kolmogorov flows and time-correlation function. *Procedia IUTAM* **5**, 244–248.
- JAMESON, ANTONY 1988 Aerodynamic design via control theory. *Journal of scientific computing* **3** (3), 233–260.
- KATOK, A B & HASSELBLATT, B A 1997 *Introduction to the Modern Theory of Dynamical Systems, Encyclopedia of Mathematics and its Applications*, vol. 54. Cambridge University Press.
- KEEFE, LAURENCE, MOIN, PARVIZ & KIM, JOHN 1992 The dimension of attractors underlying periodic turbulent poiseuille flow. *Journal of Fluid Mechanics* **242** (29), 1–29.
- MITTAL, RAJAT & BALACHANDAR, S. 1996 Direct Numerical Simulation of Flow Past Elliptic Cylinders. *Journal of Computational Physics* **367** (124), 351–367.
- NI, ANGXIU 2018a Adjoint sensitivity analysis on chaotic dynamical systems by Non-Intrusive Least Squares Adjoint Shadowing (NILSAS). *arXiv:1801.08674* pp. 1–44.
- NI, ANGXIU 2018b Adjoint shadowing directions in hyperbolic systems for sensitivity analysis. *arXiv:1807.05568* pp. 1–23.
- NI, ANGXIU, BLONIGAN, PATRICK J, CHATER, MARIO, WANG, QIQI & ZHANG, ZHICHAO 2016 Sensitivity analysis on chaotic dynamical system by Non-Intrusive Least Square Shadowing (NI-LSS). In *46th AIAA Fluid Dynamics Conference, AIAA AVIATION Forum*, pp. 1–16. American Institute of Aeronautics and Astronautics.
- NI, ANGXIU & WANG, QIQI 2017 Sensitivity analysis on chaotic dynamical systems by Non-Intrusive Least Squares Shadowing (NILSS). *Journal of Computational Physics* **347**, 56–77.
- NI, ANGXIU, WANG, QIQI, FERNANDEZ, PABLO & TALNIKAR, CHAITANYA 2018 Sensitivity analysis on chaotic dynamical systems by Finite Difference Non-Intrusive Least Squares Shadowing (FD-NILSS). *arxiv:1711.06633* pp. 1–21.
- PARISH, ERIC J. & DURAISAMY, KARTHIK 2017 A dynamic subgrid scale model for Large Eddy Simulations based on the MoriZwanzig formalism. *Journal of Computational Physics* **349**, 154–175, arXiv: 1611.02143.
- PILYUGIN, S. YU 1997 Shadowing in Structurally Stable Flows. *Journal of Differential Equations* **140** (2), 238–265.
- PILYUGIN, SERGEI YU 1999 *Shadowing in Dynamical Systems, Lecture Notes in Mathematics*, vol. 1706. Springer.
- POINSOT, T J & LELEF, S K 1992 Boundary conditions for direct simulations of compressible viscous flows. *Journal of Computational Physics* **101** (1), 104–129.
- REICK, CHRISTIAN H. 2002 Linear response of the Lorenz system. *Physical Review E - Statistical Physics, Plasmas, Fluids, and Related Interdisciplinary Topics* **66** (3), 1–11.
- RUELLE, DAVID 1980 Measures Describing a Turbulent Flow. *Annals of the New York Academy of Sciences* **357** (1), 1–9.
- RUELLE, DAVID 1997 Differentiation of SRB States. *Commun. Math. Phys* **187**, 227–241.
- RUELLE, DAVID 2008 Differentiation of SRB states for hyperbolic flows. *Ergodic Theory and Dynamical Systems* **28** (02), 613–631.
- SIEBER, MICHAEL 1987 Experiments on the attractor-dimension for turbulent pipe flow. *Physics Letters A* **122** (9), 467–470.

- THEPAUT, JEAN-NOEL & COURTIER, PHILIPPE 1991 Four-dimensional variational data assimilation using the adjoint of a multilevel primitive-equation model. *Quarterly Journal of the Royal Meteorological Society* **117** (502), 1225–1254.
- TROMP, JEROEN, TAPE, CARL & LIU, QINYA 2005 Seismic tomography, adjoint methods, time reversal and banana-doughnut kernels. *Geophys. J. Int* **160**, 195–216.
- WANG, QIQI 2014 Convergence of the Least Squares Shadowing Method for Computing Derivative of Ergodic Averages. *SIAM Journal on Numerical Analysis* **52** (1), 156–170, arXiv: arXiv:1304.3635v7.
- WANG, QIQI, HU, RUI & BLONIGAN, PATRICK 2014 Least Squares Shadowing sensitivity analysis of chaotic limit cycle oscillations. *Journal of Computational Physics* **267**, 210–224.
- WILLIAMSON, C. H. K. & ROSHKO, A. 1990 Measurements of base pressure in the wake of a cylinder at low Reynolds numbers. *Zeitschrift für Flugwissenschaften und Weltraumforschung* **14**, 38–46.
- XU, M & PAUL, M R 2016 Covariant Lyapunov vectors of chaotic Rayleigh-Bénard convection. *Physical Review E* **93** (6), 1–12.
- YOUNG, LAI-SANG 2002 What are SRB measures, and which dynamical systems have them? *Journal of Statistical Physics* **108** (5), 733–754.
- YOUNG, LAI-SANG 2003 Entropy in Dynamical Systems. *Entropy* pp. 313–327.